Water soluble chromenylium dyes for shortwave infrared imaging in mice

Shang Jia,[1,2] Eric Y. Lin,[1] Irene Lim,[1] Emily B. Mobley,[1] Lei Guo,[3,4] Ellen M. Sletten[1,*]

[1] Department of Chemistry and Biochemistry, University of California, Los Angeles, Los Angeles, CA 90095, United States

[2] Present address: Department of Chemistry and Biochemistry, University of Arkansas, Fayetteville, Fayetteville, AR 72701, United States

[3] Linde-Robinson Laboratories, California Institute of Technology, Pasadena, CA 91125, United States

[4] Present address: Department of Civil Engineering, University of Arkansas, Fayetteville, Fayetteville, AR 72701, United States

* Correspondence: sletten@chem.ucla.edu

ABSTRACT: *In vivo* imaging using shortwave infrared light (SWIR, 1000-2000 nm) benefits from deeper penetration depths, decreased background autofluorescence, and high resolution. However, the development of biocompatible contrast agents for these low energy wavelengths has significant challenges. While there have been significant advances in SWIR chromophore scaffolds over the past 5 years, a major barrier for widespread utility of SWIR small molecule fluorophores is their hydrophobicity and tendency to form non-emissive aggregates. Here, we report a platform for generating a panel of soluble and functional dyes for SWIR imaging by late-stage functionalization of a fluorophore intermediate via click chemistry. The resulting fluorophores with sulfonate, ammonium or zwitterion functionalities are all water soluble with bright SWIR fluorescence in serum, allowing for fast imaging in mice. Specifically, the sulfonate-carrying derivative enables clear video-rate imaging of vasculature with as little as 0.05 nmol injected dye, and the ammonium-modified dye shows strong retention in cells that enables tracking of xenograft tumor growth. We further showcase the versatility of this design by incorporating phosphonate functionalities for imaging of bone in awake and moving mice. This modular design of functional SWIR fluorophores in water provides insights for facile derivatization of existing fluorophores to introduce solubility and bioactivity towards bioimaging applications.

Optical imaging utilizing shortwave-infrared light (SWIR, 1000–2000 nm; also referred to as NIR-II) is a rapidly growing research area.[1–3] These long-wavelength photons benefit from reduced scattering, tissue absorption and autofluorescence compared to visible (400–700 nm) and near-infrared (NIR, 700–1000 nm) light.[4–6] These qualities render the SWIR region well-suited to assist research in small model animals and expand the scope of optical clinical diagnostics. Indeed, in 2020, 11 years after the seminal report of SWIR imaging in mice,[7] a study in humans concluded that SWIR detection was superior to NIR detection in image-guided surgery with higher tumor detection sensitivity and increased signal to noise ratio.[8] The clinical trial employed indocyanine green (**ICG**, Figure 1b), an FDA approved NIR fluorophore with a small percentage of emission in the SWIR region, as a contrast agent for their studies. If bright, SWIR analogs of **ICG** were available, the benefits of SWIR detection would be more

pronounced for these surgical guidance procedures in terms of sensitivity and accuracy. Additionally, water soluble SWIR fluorophores will expand the scope of experiments that can be performed in model organisms.

ICG is a heptamethine dye with benzo[*e*]indolium heterocycles (Figure 1b). Polymethine dyes have significant advantages as optical contrast agents including small size, biocompatibility, and excellent absorption properties (narrow absorption bands with high absorbance coefficients (ε)).[9] Consequently, polymethine dyes have seen considerable success as water soluble probes and fluorophores in the visible and NIR regions.[10–12] Over the past five years, numerous SWIR-emissive polymethine dyes have been prepared using two red-shifting strategies: polymethine chain extension [13,14] or heterocycle modification.[15–17] While each of these approaches have been successful at producing fluorophores with excellent photophysical properties for the SWIR region in organic solvent, there are significant challenges in solubilizing these large, planar, aggregation-prone fluorophores in water. Polymethine chain extension is the most classic method to red-shift this class of fluorophores, but as the chain lengths are increased, the delocalization of the π-bonds across the polymethine chain can become compromised, leading to a molecule with poly-ene character that has unfavorable photophysical properties. This phenomenon is termed ground state desymmetrization and leads to broadened absorption bands with decreased absorbance coefficients and lowered quantum yields of fluorescence.[18,19] Ground state desymmetrization is enhanced in polar aqueous media,[19] rendering imaging of long chain polymethine dyes in physiological conditions more challenging. Heterocycle modification allows for SWIR fluorophores with pentamethine or heptamethine chains, decreasing contributions from ground state desymmetrization; however, these heterocycles are often more hydrophobic than the classic indolium heterocycles and the approaches commonly used to solubilize polymethine dyes in water are not successful on these more customized heterocycles. In fact, the small number of water soluble polymethine SWIR fluorophores to date all include indolium-derived heterocycles with polymethine chain extension, and varying amounts of ground state desymmetrization are observed in water (Figure 1a).[13,14,20,21]

Here we report a modular approach to water soluble SWIR-emissive chromenylium heptamethine dyes. The chromenylium heterocycle scaffold is a bright, red-shifted heterocycle for polymethine fluorophores (*e.g.* **Flav7** and **Chrom7**, Figure 1c).[22–28] Chromenylium polymethines encapsulated in micelles have enabled SWIR imaging at record frame rates,[22–24] with multiple channels,[23,24] and using responsive FRET probes.[27] To render the chromenylium heptamethine dyes water soluble, we determined two critical modifications are necessary: steric bulk on the polymethine linker to block π-π stacking and addition of multiple charged functionalities to impart sufficient water solubility. We prepare the clickable hydrophobic fluorophore **PropChrom7**, (Figure 1d) which contains an *ortho*-methyl substituted phenyl group at the 4'-position to prevent aggregation and four propargyl groups for copper-catalyzed azide-alkyne cycloaddition (CuAAC) with charged azides to introduce hydrophilicity and/or functionality into the final product. **PropChrom7** is a versatile intermediate for the preparation of a

range of SWIR fluorophores with different functional groups and charge states. Using this approach, we obtained a panel of water soluble **Chrom7** derivatives that carry sulfonates (**SulfoChrom7**), ammoniums (**AmmonChrom7**) and zwitterions (**ZwitChrom7**) with varying localization properties (Figure 1d). These dyes all show monomeric dispersion in serum at dilute conditions with bright SWIR fluorescence. Notably, negatively-charged **SulfoChrom7** shows slow absorption by tissue which allows for imaging of superficial veins with low detection limits; quintuply positively-charged **AmmonChrom7** shows efficient uptake and prolonged retention in cells, enabling tracking of xenograft tumor growth in mouse models. We further showcased this late-stage functionalization design by incorporation of tetravalent phosphonates as both hydrophilic groups and calcium binding sites to achieve high-resolution bone imaging in both anesthetized and moving mice. We expect our platform will expand to provide water soluble SWIR fluorophores with varying photophysical properties and more bioactivity, as well as inspire more SWIR fluorophores packaged as modular building blocks to furnish complex animal imaging tools.

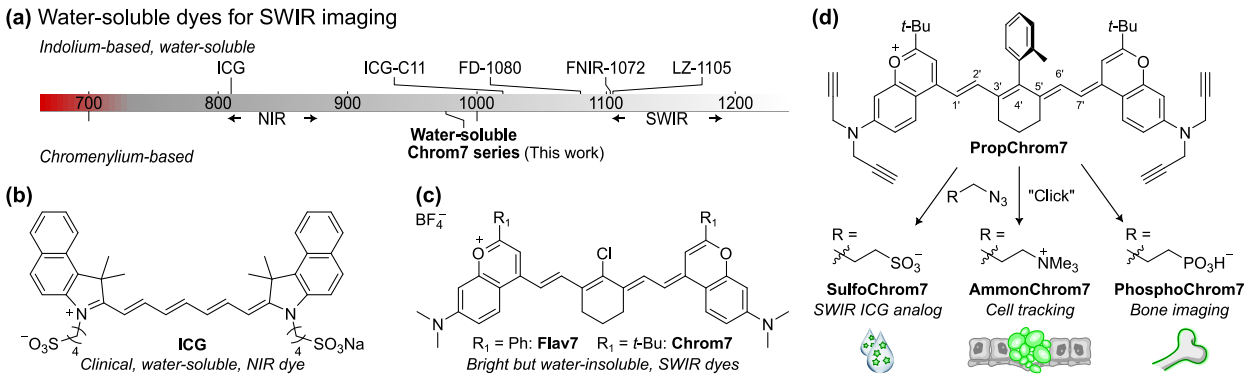

Figure 1 Design of hydrophilic and versatile Chrom7 derivatives. (a) Water soluble polymethine dyes used for SWIR imaging and their emission wavelengths. (b) Structure of **ICG**. (c) Structures of **Flav7** and **Chrom7**. (d) Derivatization of **PropChrom7** into a series of water soluble, functional SWIR imaging agents.

Results and Discussion

Design and synthesis of water soluble SWIR heptamethine dyes. When considering how to prepare water soluble derivatives of chromenylium SWIR dyes, we aimed to design a synthesis that would minimize water soluble intermediates and maximize diversity of the final fluorophores. We focused on first installing aggregation-minimizing functionalities on a hydrophobic scaffold that could then be transformed into a water soluble fluorophore through a click reaction with a charged functionality. To disfavor aggregation, we base our fluorophore on **Chrom7** as its bulky di-*tert*-butyl substitution acts as steric hindrance that disfavors aggregation compared to planar **Flav7**, as evidenced by their micelle formulations.[22,24] However, the two *tert*-butyl groups were not effective enough at reducing aggregation and an *ortho*-methylphenyl group was installed at the 4' position of the polymethine chain. This substitution is analogous to the pendent aryl ring in Tokyo Green.[29] Due to its steric demands, the 4'-

substitution is perpendicular to the dye plane, which positions its protruding methyl group close to the polymethine bridge, thus preventing another dye molecule from effective π-π stacking necessary for aggregation to occur. These aggregation-minimizing features were consolidated into a tetra-propargylated chromenylium fluorophore, deemed **PropChrom7**. To promote the aqueous solvation of the fluorophores, we introduced hydrophilicity at the very last step, where we performed CuAAC between **PropChrom7** with selected hydrophilic azides. We expect the four equivalents of hydrophiles to render the heptamethine dyes water soluble. Initially, we selected organic azides carrying sulfonate, ammonium, or zwitterion functionality.

PropChrom7 as a central building block enables the facile synthesis of the water soluble dyes in this work. The synthesis of **PropChrom7** is carried out in organic solvents similar to previously reported chromenylium dyes. It is only in the last step converting **PropChrom7** to the final water soluble fluorophore where aqueous solvent and HPLC separation were necessary (Scheme 1). Specifically, we obtained the chromone **1** from the microwave-assisted pyrone synthesis,[30] utilizing allyl protection groups on the aniline that was compatible with high temperatures and pressures encountered in microwave synthesis (Supporting Information). Following allyl group deprotection with $Pd(PPh_3)_4$, chromone **1** was obtained and the propargyl substitutions were installed by treatment with propargyl bromide to yield **2**. The standard conditions for conversion of chromones to chromenylium dyes using MeMgBr or MeLi both gave poor yields due to reactivity with the propargyl groups. We found pre-treatment with Me_2CuLi provided an *in situ* protection of the terminal alkynes, allowing isolation of **3** in 79% yield. In parallel to the synthesis of propargylated chromenylium **3,** we prepared polymethine linker **6** which contains the aggregation-blocking methyl-phenyl group. Linker **6** was constructed from Suzuki-Miyaura cross-coupling between commercially available compounds **4** and **5** at 120 °C, which is harsher than the commonly-used condition for this type of conversion to compensate for the increased steric demands. **PropChrom7** (compound **7**) was prepared from the condensation of **6** and **3** in 21% yield. This central intermediate then underwent CuAAC with hydrophilic organic azides under a commonly-used condition for bioconjugation with THTPA as the ligand,[31] but in a 1:2 mixture of water and methanol, to accommodate the solubility of both the hydrophobic dye and hydrophilic azide. This procedure resulted in **8** (**SulfoChrom7**), **9** (**AmmonChrom7**) and **10** (**ZwitChrom7**) all with ca. 59% yield.

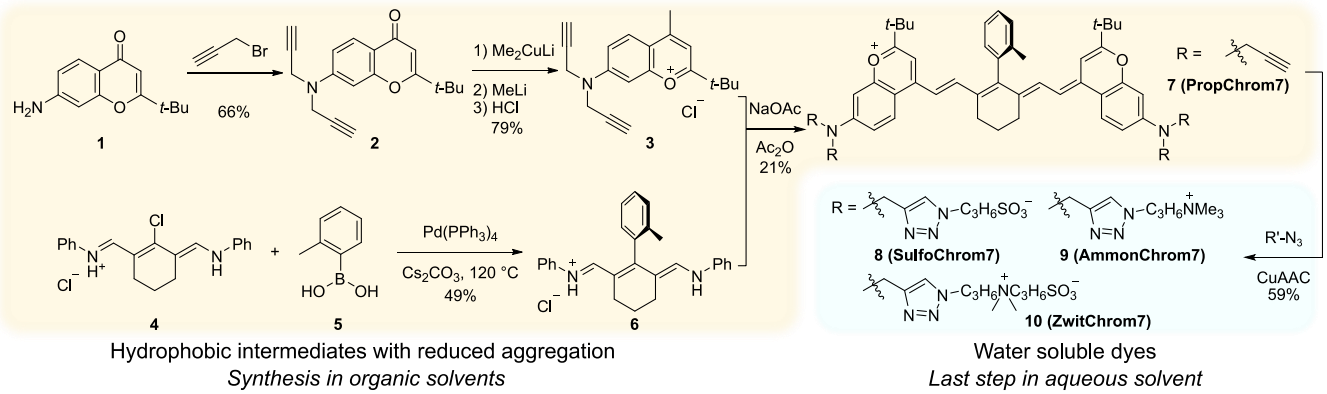

Scheme 1 Synthesis of **PropChrom7** and its post-synthetic CuAAC to afford **SulfoChrom7**, **AmmonChrom7**, **ZwitChrom7**.

***In vitro* characterization of water soluble SWIR fluorophores.** We first tested the photophysical behaviors of the dyes in different conditions (Figure 2a, S5a). All three hydrophilic dyes (**Sulfo-**, **Ammon-** and **ZwitChrom7**) and hydrophobic dye **PropChrom7** show monomeric dispersion in MeOH and can be compared directly (Figure 2a, S1-S4). By converting the propargyl groups on **PropChrom7** to the triazolemethyl groups, the fluorophore exhibits a 10 nm red-shift in absorption and a 16 nm red-shift in emission maxima, corresponding to the increased electron donation from the triazoles (Figure 2a,d, S1-S4). Most importantly, all the hydrophilic dyes exhibit similar properties in absorption maximum and extinction coefficient, as well as fluorescent quantum yield (Figure 2a,d,e), suggesting that the functionality appended to **PropChrom7** can be varied without compromising the photophysical properties.

Owing to the structural homology of **8–10**, we are able to compare the water-solubilizing ability of sulfonate, ammonium, and zwitterion functionalities. As shown in the absorption spectrum in H_2O, ammonium salt possesses the strongest ability to solubilize the chromenylium fluorophore as evidenced by the dominant monomeric absorption profile of **AmmonChrom7** at concentrations as high as 2 μM (Figure S3b,d). Next best is the sulfonate group in **SulfoChrom7** which shows a discernible monomer absorption (Figure S2b,d), whereas zwitterionic moiety in **ZwitChrom7** is primarily aggregated in water (Figure S4b,d). While the dyes do display some aggregation in water, gratifyingly, there is minimal evidence of ground-state desymmetrization in H_2O, suggesting an advantage of heptamethine SWIR dyes (Figure S5d).

Next, we evaluated the fluorophores in more biologically relevant fetal bovine serum (FBS) and found that all three fluorophores displayed a well-defined monomeric absorption and emission characteristic of polymethine dyes (Figure 2e). **AmmonChrom7** aggregates the least in FBS with monomeric absorption observed up to 32 μM, while **SulfoChrom7** and **ZwitChrom7** have dominant monomeric absorption up

to 8 μM. Additionally, in FBS the absorbance of the three dyes were red-shifted by ca. 40 nm (Figure 2e). These observations suggest that all three fluorophores are interacting with serum proteins, which is a behavior similar to that seen for **ICG**.[32] The quantum yield values for **AmmonChrom7** and **SulfoChrom7** are above 0.5% in FBS, a notable metric for SWIR dyes in aqueous media. The **ZwitChrom7** is slightly lower at 0.32% in FBS. Comparative capillary images in FBS between **AmmonChrom7, SulfoChrom7, ZwitChrom7,** and **ICG** with 785 nm or 975 nm excitation suggest all three SWIR dyes are comparable or superior to **ICG** for SWIR imaging (Figure 2b,c).

(a)

Fluorophore	Solvent	$\lambda_{max,abs}$ / nm	ε_{max} / 10^4 $M^{-1}cm^{-1}$	$\lambda_{max,ems}$ / nm	Φ_F / %
PropChrom7	MeOH	928	14	946	1.18
SulfoChrom7	MeOH	938	16.5	964	1.06
	FBS	963	9.5	976	0.56
AmmonChrom7	MeOH	938	16	962	1.18
	H_2O	923	6.2	940	0.43
	FBS	962	11	977	0.58
ZwitChrom7	MeOH	940	16.4	965	1.01
	FBS	960	11.5	975	0.32

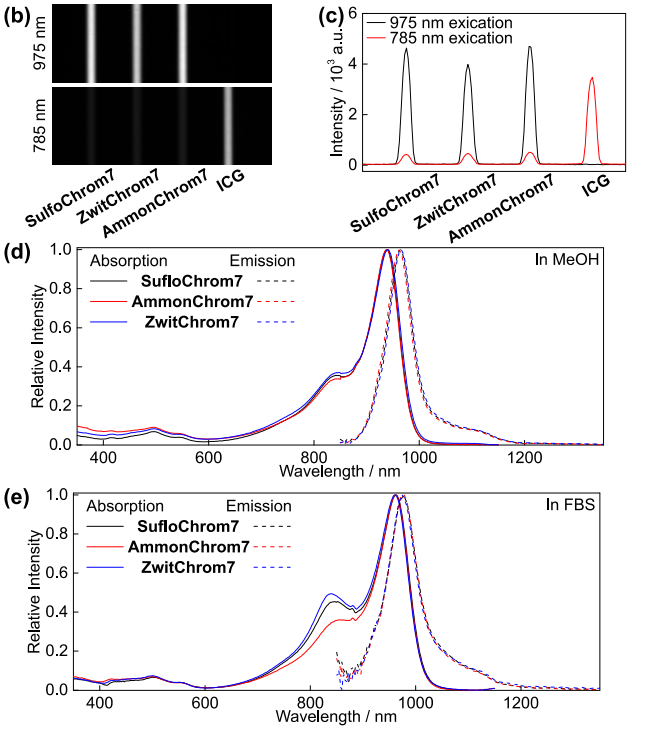

Figure 2 Photophysical comparisons of water soluble SWIR fluorophores. (a) Table of photophysical properties. See Figure S5a for error values. (b) Brightness comparison by SWIR imaging at 4ms/frame of each water soluble dye (2 μM) in FBS in capillaries under 975 nm illumination (100 mW/cm^2), with 2 μM of ICG in FBS under 785 nm illumination (50 mW/cm^2) as a benchmark. (c) Quantification of (b). (d,e) Overlay of absorption (solid line) and emission (dotted line) spectra of 2 μM **Sulfo-**, **Ammon-** or **ZwitChrom7** in methanol (d) or FBS (e).

We further tested the dyes for their biocompatibility. The hydrophilic dyes display reasonable stability,

with around 1/2 of **SulfoChrom7**, 1/4 of **AmmonChrom7** and 1/10 of **ZwitChrom7** left over 2 days at 37 °C in FBS (Figure S5b), which is in the same range as the degradation of ICG.[33,34] The major degradation pathway of these dyes is attributed to oxidation of the fluorophore as determined by LC/MS. Inhibition of proliferation in HEK293 cells is minimal for **AmmonChrom7** even with dye concentrations as high as 100 μM over 18 h, and the growth inhibition of **SulfoChrom7** and **AmmonChrom7** are also mild at 20 μM (<15% inhibition, Figure S5c). As such, we deem these dyes suitable for use in animals at or below ca. 10 μM (20 nmol injection for 5-week or older mice) concentrations.

Biodistribution of water soluble SWIR fluorophores. After *in vitro* characterization, we carried out *in vivo* imaging of the three hydrophilic dyes in mice to compare the differences in biodistribution. Towards this end, we injected 20 nmol of each dye into the tail vein, and observed a strong fluorescence signal for each dye which allowed imaging at 100 frames per second (fps, 0.5-2 ms exposure time, Figure S6-S8) through an 1100 nm long-pass (LP) filter. All three dyes initially localized primarily in the liver and vasculature. After 3 h, almost all **AmmonChrom7** accumulated in liver (Figure S7a-d), whereas **SulfoChrom7** and **ZwitChrom7** showed diffuse signal through the mouse body, but still with substantial liver accumulation (Figure S6a-d; S8a-d). The distribution and brightness of all three dyes remain relatively unchanged over two days (Figure S6g,S7g,S8g), indicating that they are not actively metabolized or secreted. In fact, their lasting fluorescence signals were retained much beyond their half-life in aerated FBS, suggesting significantly reduced degradation *in vivo*. Dissection of the organs 48 h after injection reveals that all the dyes stained primarily the liver (Figure S6e,f; S7e,f; S8e,f). While **AmmonChrom7** displays the strongest accumulation in the liver as noted, all three dyes showed some staining in the kidney and intestine, suggesting slow clearance through these pathways. Compared with **ICG**, which has a blood $t_{1/2}$ of 10 min [35] followed by hepatobiliary clearance within 6 h,[21,36] the lasting *in vivo* fluorescence of our dyes offers a valuable reference for the future development of SWIR contrasting agents. The slower pharmacokinetics may enable flexible introduction time before clinical imaging. The long circulation time of these fluorophores also makes them ideal for long-term tracking of biological events in living mice for research purposes.

Systemic imaging with SulfoChrom7. The anionic **SulfoChrom7** is the most similar of the fluorophores to **ICG**, the current benchmark for untargeted optical *in vivo* imaging, and appeared the brightest of the fluorophores in capillary imaging experiments. For these reasons, we performed a more extensive set of *in vivo* imaging experiments with **SulfoChrom7** to determine its limit of detection and performance in comparison to **ICG.** Current clinics usually apply 2.5 mg (ca. 0.05 μmol/kg) ICG for detection of lymph nodes, tumors and vital structures under routine NIR imaging,[37] whereas for SWIR imaging a much larger dose of **ICG** is required to compensate for the small fraction of the SWIR emission from **ICG** (0.3 or 0.6 μmol/kg in mouse, pig or human) but still with >100 ms exposure time.[8,21,36,38] Considering that **SulfoChrom7** is a bright fluorophore with majority of emission in the SWIR, we anticipate a very small dose of **SulfoChrom7** is necessary for SWIR imaging. This represents

an advance over **ICG**, since it is beneficial to introduce as little contrast agent as possible to minimize unnatural interactions and toxicity. To determine the relevant concentrations necessary for SWIR imaging with **SulfoChrom7,** we performed sequential tail vein injections of 0.05 nmol (ca. 2.5 nmol/kg) of **SulfoChrom7.** We set our desired imaging parameters at 33 fps (real time imaging) first with an 1100 nm LP filter (Figure 3a). As soon as the first dose of 0.05 nmol dye was introduced, the liver lit up together with discernible saphenous and medial marginal veins, facial veins and abdominal wall veins (Figure 3b,d). As more dye was injected, the signal increased in a dose-dependent manner, giving rise to higher signal to noise ratio (Figure 3d, S9a-f, Video S1). This is, to the best of our knowledge, the smallest amount of dye directly administered without formulation to enable high quality video-frame rate non-invasive imaging.

We then performed a similar set of experiments with more restrictive imaging metrics of 33 fps and a 1400 LP filter. Water molecules have considerable absorption of light beyond 1400 nm, which reduces signal from deeper tissue and at the same time enhances the resolution by attenuating scattered light (Figure 3a).[39] For these experiments, we increased the amount of dye injected to 4 × 2.5 nmol to compensate for the reduced integrated signal after 1400 nm (Figure S2c) as well as the signal loss from water absorption. After 5.0 nmol dye was introduced, the fluorescence image clearly delineated a map of the vein system of the mouse, whereas the interference from liver accumulation was reduced due to the more significant depth of the liver (Figure 3c,d). As the amount of dye was increased, fluorescence signals increased with a more distinct vein map and reduced noise level (Figure 3d, S9g-l, Video S2). With 10 nmol **SulfoChrom7**, we were able to obtain a detailed image of superficial vasculature with minimal noise level (Figure S9j). On the other hand, while **ICG** also lit up the vein system, the contrast was much weaker than **SulfoChrom7** under the same settings because of the tiny emission tail at 1100 nm or longer wavelengths for SWIR imaging. Moreover, the observation window is much shorter, which we further assessed in the next step where we performed a direct comparison of **SulfoChrom7** and **ICG** for vasculature imaging.

We are able to directly compare **ICG** and **SulfoChrom7** as SWIR contrast agents in the same mouse because they can be selectively excited at different wavelengths (Figure 3e, 785 nm for **ICG**, 975 nm for **SulfoChrom7**). For these experiments, we used a 1300 LP filter to compromise between resolution and signal intensity. As shown in the fluorescence image, immediately after injection, both dyes stained the vasculature with much stronger signal in the **SulfoChrom7** channel owing to its red-shifted emission (Figure 3f,h). Within 30 min, most ICG accumulated in the liver with secretion into the intestine, leaving negligible signal in the mouse body, whereas **SulfoChrom7** still reflected the superficial vasculature map while also displaying liver accumulation (Figure 3g,h). **SulfoChrom7** displayed an increasing brightness ratio over ICG in veins over time (up to 7-8 fold, Figure S10e-h). A similar trend is also displayed when imaging with 1100 or 1400 nm LP filter, where signals from **SulfoChrom7** are retained in vasculature during the 33 min time frame while ICG clears into the liver and intestines (Figure S10a-d,i-l). Taken together, **SulfoChrom7** benefits from its higher SWIR brightness and longer blood

circulation time than ICG, suggesting itself as an excellent SWIR fluorophore to visualize the superficial vein system over long periods of time with high sensitivity and adjustable resolution in different imaging setups.

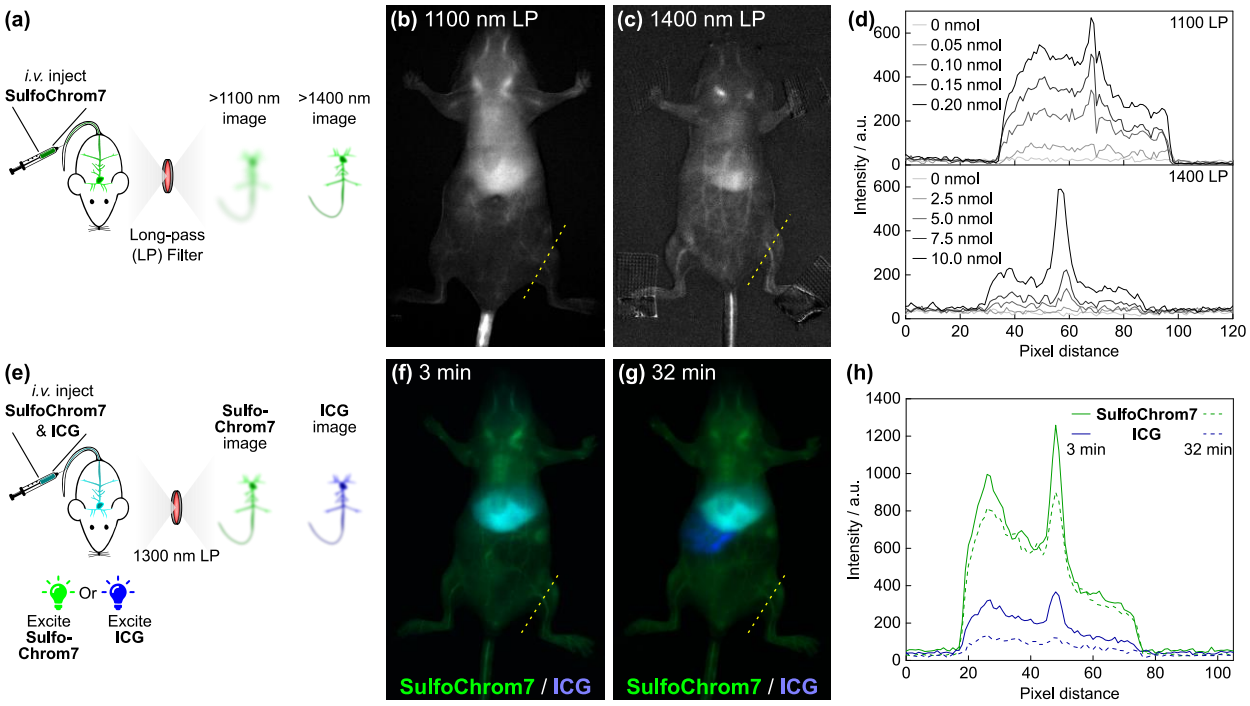

Figure 3 Video-rate imaging of mouse vasculature with of *i.v.* injected **SulfoChrom7**. (a) Schematics of *i.v.* injection of **SulfoChrom7** for vasculature imaging under different filters. (b-d) Fluorescence images of mice recorded at 30 ms/frame (b) under 1100 nm LP filter with 0.05 nmol dye (20 frames averaged, max brightness 646 excluding tail region), or (c) under 1400 nm LP filter with 5.0 nmol dye (20 frames averaged, max brightness 289 excluding tail region); their raw brightness profiles along the highlighted line is shown in (d). (e) Schematics of co-injection of **SulfoChrom7** and **ICG** for their direct comparison under two-channel imaging. (f-h) Fluorescent images of a mouse at 10 ms/frame under 1300 nm LP filter (f) 3 min [84 frames averaged, max brightness 4302 (green) and 3960 (blue)] or (g) 32 min [87 frames averaged, max brightness 3692 (green) and 4027 (blue)] after *i.v.* injection of **SulfoChrom7** (10 nmol, shown in green) and **ICG** (10 nmol, shown in blue); their raw brightness profiles along the highlighted line is shown in (h). Illumination was provided at 100 mW/cm^2 for 975 nm and 50 mW/cm^2 for 785 mm.

Tracking of tumor growth with AmmonChrom7. Next, we explored the utility of the highly cationic **AmmonChrom7** fluorophore. **AmmonChrom7** features a permanent z = +5 and m/z of 269.6. This high charge density is close to those of some cell-penetrating peptides (*e.g.* nonaarginine m/z=159 at z=8, TAT peptide m/z=233 at z=7), suggesting its effective internalization into cells. Highly-cationic dye molecules have also shown effective cellular uptake and find utility in cell tracking applications,[40,41]

whereas many positively-charged nanoparticles has been developed for such purpose.[42] We thus anticipated that **AmmonChrom7** could be similarly internalized into cells for long-term visualization (Figure 4a). To test this hypothesis, we incubated HEK293 cells with 50 μM of **AmmonChrom7, SulfoChrom7,** and **ZwitChrom7** and analyzed the absorbance of cell lysates over time. We found significant absorbance for cells treated with **AmmonChrom7**, whereas the signal for **SulfoChrom7** and **ZwitChrom7** is minimal (Figure S11a,b). The cellular labeling of **AmmonChrom7** dropped significantly on the first day after staining, possibly due to exocytosis from saturated cytosol, and then decreased fairly slowly to retain a signal around 50-70% over five days (Figure 4b). Similar behavior was also observed in A375 cells, a human melanoma cell line, and SK-OV-3 cells, a human ovarian cancer cell line (Figure 4b). These data, in combination with the low cytotoxicity (Figure S5c), slow clearance (Figure S7), non-aggregation behavior and high SWIR brightness in aqueous solutions (Figure 2a,d,e; S3) make **AmmonChrom7** a great candidate for cell tracking experiments.

To showcase the excellent retention of **AmmonChrom7** in cell tracking experiments, we monitored the *in vivo* growth of xenograft tumors in mice. We first stained A375 cells with 50 μM **AmmonChrom7** for 18 h prior to their *s.c.* injection into the left flank of mice to track their growth as xenograft tumors (Figure 4a), with non-stained cells injected to the right flank as control. The stained cells initially showed spread out and smeared fluorescent distribution upon injection (Figure 4c, S12a), and then became coagulated within the first two weeks, corresponding to the assimilation of Matrigel that initially supported the cells (Figure 4c, S12b). In the meantime, the brightness of the stained tumor increased corresponding to the increased dye density, allowing for image capturing with as short as 1 ms exposure time (Figure S12g). As the cells started to divide, the size of the fluorescence area gradually increased, which correlates well with the caliper measurement (Figure 4c). While the overall mean fluorescence decreased upon tumor growth due to the dilution of the dye (Figure S12g), some regions of the tumor showed lower signals (Figure 4d, S12c,d), possibly as indicators of actively-growing sites versus more senescent locations of the tumor. Notably, the fluorescence signal was well-contained at tumor sites as seen in the bright-field image (Figure 4d, S12b-d). We sacrificed the mice at varying dates depending on the size of the two tumors to obtain *ex vivo* images. As expected, the three stained tumors all showed bright fluorescence under SWIR camera, whereas we observed much lower fluorescence in the surrounding tissue, negligible intensity in the liver, and essentially no fluorescence in the control tumors and the rest of the body (Figure 4e-g). These results further confirm that **AmmonChrom7** was contained at the tumor site during their growth with negligible leakage. Additionally, the 3/3 take rate and comparable growing speed (Figure S12h) suggest an insignificant long-term inhibition effect of **AmmonChrom7** to the A375 tumor growth.

Next, we performed a similar experiment with the more challenging, slow growing, xenograft model SK-OV-3. We treated SK-OV-3 cells with 50 μM **AmmonChrom7** prior to *s.c.* injection in the flank and abdomen of three mice. Again, the fluorescence signal showed clear overlap with the tumor location from bright-field images (Figure S13a,b). The size of the tumors remained largely unchanged since

week 1, and the fluorescence intensity fluctuated accordingly, rather than decreasing (Figure S13d-f), suggesting that the dye was retained at the tumor site with little diffusion or degradation over the 38-day period. To our knowledge, this sets the record for the longest time period for a SWIR dye to be monitored *in vivo*. To confirm that the fluorescence originated from the tumor, we injected OTL-38, a recently FDA-approved NIR dye that labels the overexpressed folate receptor [43] on SK-OV-3 cells. OTL-38 contains a NIR heptamethine analogous to ICG as the fluorophore core and thus we envisioned the tail emission in the SWIR could be utilized for imaging (Figure S13c). As expected, clear colocalization was observed in *in vivo* images (Figure S13a,b) and *ex vivo* images (Figure 4h), supporting that the dye continuously labels the SK-OV-3 tumor throughout the period of the experiment. While much non-specific accumulation of OTL-38 was observed in other organs, **AmmonChrom7** showed clear staining of the tumor with very little diffusion into the surrounding tissue (Figure 4h,i, S13g-i), highlighting the cell tracking potential of **AmmonChrom7**. Taken together, these experiments demonstrate that by incorporating multiple positive charges onto our dye scaffold, we successfully engineered AmmonChrom7 as a cellular stain for the long-term tracking of tumor growth, offering the first small molecule option for *in vivo* cell tracking using SWIR imaging. The high brightness and minimal cell growth inhibition provide a valuable tool for studying cancer models, as well as potential use in stem cell and immune cell research.

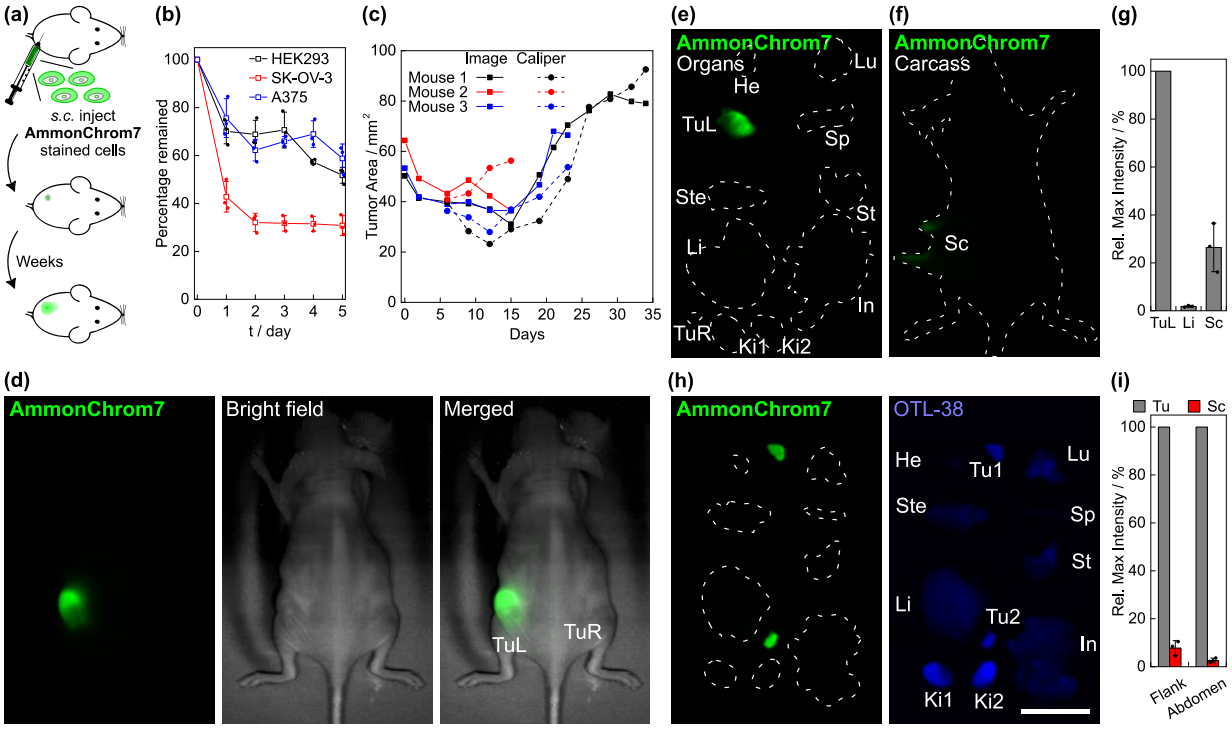

Figure 4 Tracking of tumor xenograft growth using **AmmonChrom7**. (a) Schematics of *s.c.* injection of **AmmonChrom7** stained cells for tracking of their *in vivo* growth. (b) Uptake and retention of **AmmonChrom7** in different cell lines. (c) Comparison of the growth curves of stained A375 as determined by fluorescence imaging and by caliper measurement in three mice. (d) *In vivo* images of A375 tumors 34 days after xenograft on Mouse 1 (1 ms/frame, 31 frames averaged, max brightness

7957). (e, f) *Ex vivo* fluorescent images of A375 tumors and organs (e) and carcass (f) of Mouse 1 34 days after xenograft [0.8 ms/frame, 51 frames averaged, max brightness 10873 (e) and 2920 (f)]. See Figure S12e,f for corresponding bright field images. Lu: lung, Sp: spleen, St: stomach, In: intestine, He: heart, Ste: sternum, Li: liver, Ki: kidney. TuL: left, stained tumor. TuR: right, unstained tumor. Sc: subcutaneous tissue around TuL. (g) Maximum brightness of *ex vivo* fluorescent tumor, liver and subcutaneous tissue surrounding the tumor (mean ± s.d., Mouse 1: 34 days, Mouse 2: 15 days, Mouse 3: 23 days after xenograft). (h) *Ex vivo* fluorescent images of SK-OV-3 tumors and organs 39 days after xenograft and 4 h after *i.v.* injection of OTL-38 [1 ms/frame, 112 frames averaged, max brightness 9928 (green) and 2095 (blue)]. See Figure S13g for corresponding bright field image. Tu1: abdomen *s.c.* tumor. Tu2: flank *s.c.* tumor. (i) Maximum fluorescence intensity of *ex vivo* tumors and their surrounding hypodermis after tumor removal from the sacrificed mice (n = 3, mean ± s.d., 39 days after xenograft). Illumination was provided at 100 mW/cm^2 for 975 nm and 50 mW/cm^2 for 785 mm. Scale bar: 2 cm.

Targeted imaging with water soluble SWIR fluorophores. Initially, we focused on appending functionality to **PropChrom7** that would induce water-solubility; however, a major advantage of **PropChrom7** is the versatility of functionality that can be appended onto the SWIR chromophore. To showcase this, we prepared **11** (**PhosphoChrom7**) for bone-targeted imaging (Figure 5a). Four phosphate groups were clicked onto **PropChrom7** in 20% yield with the phosphate groups playing a dual role of hydrophilic and Ca^{2+}-binding moieties. The unique binding affinity of phosphonates towards divalent metals has previously been harnessed in development of bone-targeting drugs [44] and NIR bone imaging agents.[45–47] We thus anticipated that **PhosphoChrom7**, with its four phosphonates, could be delivered without a carrier and facilitate skeleton imaging due to its affinity for bone.

We first analyzed **PhosphoChrom7** in *in vitro* assays. The solubility of this compound in FBS is lower than the **Sulfo-**, **Ammon-**, or **ZwitChrom7** (Figure S14). The lower solubility is consistent with trends seen for bisphosphonate drugs. The photophysical consequences of the decreased solubility is a broad aggregation peak at 760 nm. Interestingly, this aggregate peak is significantly blue-shifted compared to the other three water soluble dyes, suggesting a different mode of aggregation induced by the phosphonate moieties (Figure 5b, S14). Conversely, the absorption/emission wavelengths of the monomer peak are almost identical to the other three dyes (Figure 5b, S5a), providing further evidence that the functionality attached to **PropChrom7** does not drastically affect the photophysical properties of monomeric fluorophore core.

We tested the binding affinity towards hydroxyapatite, the major mineral component of bone. Incubation with **PhosphoChrom7** in bovine serum led to a bright suspension of the particles under SWIR camera, and most importantly, sequential washes with bovine serum only slightly decreases the overall brightness, indicating strong binding affinity of **PhosphoChrom7** towards hydroxyapatite (Figure 5c). To rule out the possibility of co-precipitation of the dye with the hydroxyapatite powder due to its

limited solubility, we performed scanning electron microscopy on the particles. While we were unable to observe standalone particles without calcium and phosphorus after dye-treatment, we detected a significant increase of carbon element in energy dispersive X-ray spectrometry (EDS) mapping for the dye-treated particles compared to untreated ones (Figure S15), suggesting that the dye was indeed adsorbed onto the calcium salt. The toxicity of **PhosphoChrom7** is also mild at low concentrations (Figure S5c), similar to **Sulfo-** and **ZwitChrom7**. Collectively, these properties of **PhosphoChrom7** meet the criteria for bone-targeted SWIR imaging.

We then performed mouse imaging using this tetraphosphonate SWIR fluorophore. After *i.v.* injection, **PhosphoChrom7** initially localized in the vasculature (Figure S16a,f), but gradually redistributed and began to feature bone structures at 8 h (Figure S16b,g), along with some accumulation in the liver. Aside from strong liver staining, the reduction of non-bone-localized signals gave rise to a contour of mouse skeleton after 24 h or 48 h (Figure 5d-f, S16c,d,h,i) with slightly faster clearance compared to previous hydrophilic dyes (Figure S16n). While the dye may localize more onto bone regions with higher osteoblast or circulation activity, the SWIR image clearly outlines the mandible, sternum, tibia and phalange bones on the ventral view (Figure 5d) and maxilla and vertebra on the dorsal side (Figure 5e). The rib cage can be clearly visualized on the lateral view when the skin was gently lifted around the shoulder to reduce skin scattering (Figure 5f). The high brightness of **PhosphoChrom7** also enables bone imaging in awake and moving mice with comparable details (Figure 5g, Video S3). Most importantly, all these features were readily identifiable with high resolution in living mice without skin removal. Nonetheless, when the skin was removed from an euthanized mouse, more details of its bone structure were revealed (Figure S16e,j). Images of the dissected organs indicate that although bone was clearly stained by **PhosphoChrom7**, the liver is the major target of the dye similar to our other hydrophilic dyes (Figure S16l,m). We further removed the abdominal organs to eliminate their interference and were able to obtain a high-contrast image of the skeleton of the mouse (Figure 5h, S16k). Collectively, by facile introduction of calcium-binding phosphonates to our tetravalent functionalization platform, **PhosphoChrom7** stands out as the first reported bone-targeting SWIR fluorophore. **PhosphoChrom7** enables non-invasive optical imaging of bone at video rate speeds, providing a platform for studying osteology and bone-related diseases in model animals.

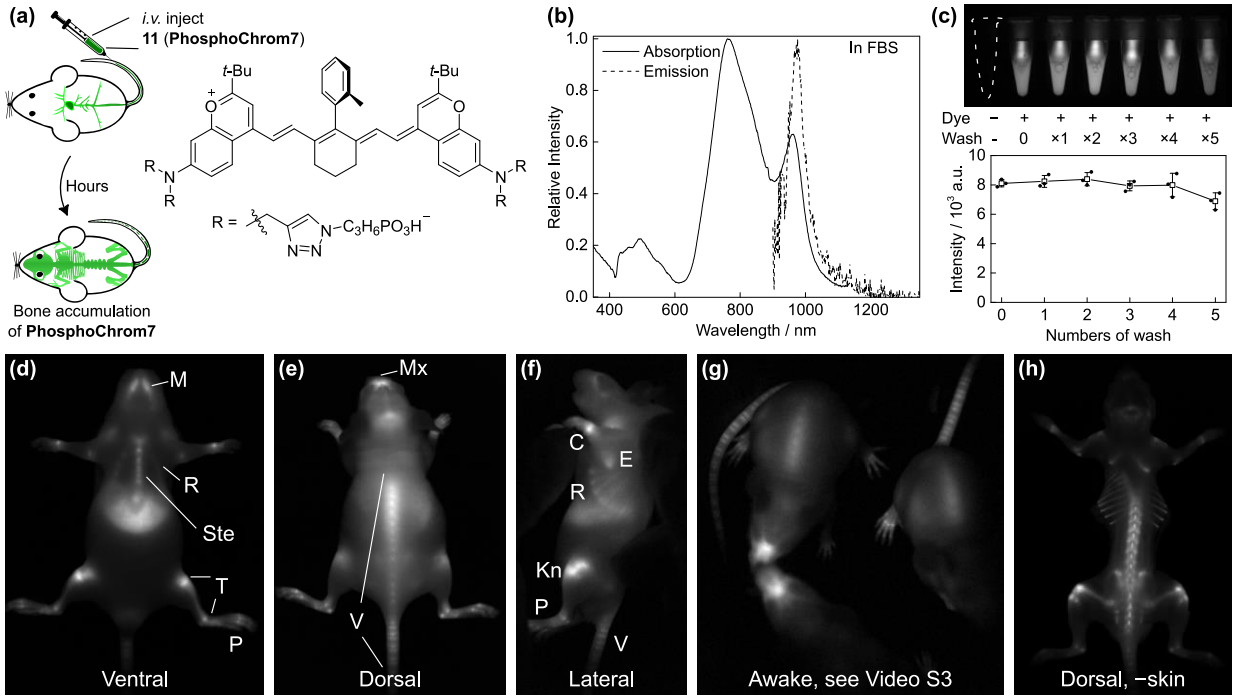

Figure 5 Imaging of bone using **PhosphoChrom7**. (a) Schematics of bone imaging by *s.c.* injection of **PhosphoChrom7**. (b) Absorption and emission spectra of 2 μM **PhosphoChrom7** in FBS. (c) Fluorescent image of calcium hydroxyapatite suspension in bovine serum treated with **PhosphoChrom7**, and its subsequent washes with bovine serum (0.5 ms/frame, 101 frames averaged, max brightness 11338); quantification is shown below (mean ± s.d., n = 3). (d-f) Fluorescence images of a mouse 24 h after *i.v.* injection of 20 nmol **PhosphoChrom7** on (d) ventral, (e) dorsal or (f) lateral view. M: mandible, Mx: maxilla, R: Rib, Ste: sternum, T: tibia, P: phalange, V: vertebrae, C: carpus, E: elbow, Kn: knee. (g) Representative single frame from Video S3 showing fluorescence image of awake mice 48 h after injection. (h) Fluorescence images of a mouse after removal of abdominal organs and most of skin on dorsal view. Images were captured under 100 mW/cm^2 975 nm illumination at 3 ms/frame (d-h); 81 frames (d-e), single frame (f-g) or 201 frames (h) averaged. Max brightness: 7096 (d), 4985 (e), 6379 (f), 6962 (g) and 12313 (h).

Concluding remarks

To close, we herein have reported a modular platform that uses **PropChrom7** as a central intermediate with four conjugation handles to easily access a series of functionalized SWIR fluorophores via CuAAC. Through this platform, we obtained **Sulfo-**, **Ammon-**, **Zwit-** and **PhosphoChrom7** as hydrophilic / water soluble SWIR dyes. All these dyes display minimal aggregation and ground state desymmetrization in serum. They exhibit bright SWIR fluorescence when *i.v.* injected in mice and can be imaged with video frame rates. Notably, these dyes readily dissolve in buffer as homogeneous solutions for convenient, direct administration, without concerns of batch variation, storage instability or potential *in vivo* breakdown which are frequently encountered for micelle formulations.

Besides the increased hydrophilicity imparted by the click reaction, this family of SWIR fluorophores

offers versatile imaging tools. In particular, the anionic dye **SulfoChrom7** stands out as a red-shifted analog of **ICG** with greatly enhanced SWIR brightness and longer circulation time. **SulfoChrom7** facilitates imaging of mouse liver and vasculature with as little as 0.05 nmol, the smallest amount reported of contrast agents that enabled video rate imaging. The cationic dye **AmmonChrom7** enables the monitoring of xenograft tumor growth over weeks with minimal signal loss and little diffusion into other tissues owing to its excellent brightness, biocompatibility, *in vivo* stability and cellular retention. Our tumor tracking experiments also set the record of *in vivo* detection time length for SWIR dyes. The cell tracking capability of this dye has the potential for use in monitoring cell activities in *in vivo* studies on tumorigenesis and immune cell migration. Lastly, **PhosphoChrom7** exhibits strong binding to calcium minerals due to the four phosphonate groups on the molecule, furnishing the first bone-targeting fluorophore in the SWIR. Its brightness and reduced scattering of SWIR light eliminate the need for sacrificing, skinning or even anesthesia of the mice for high resolution bone imaging, enabling non-invasive video recording of the skeleton in awake, moving mice.

Our design also serves as a starting point for the modular design of water soluble, functional and formulation-free SWIR fluorophores for *in vivo* imaging. By separating the fluorophore synthesis and the introduction of water-solubility and/or bioactivity, this late-stage modification method allows for the facile combination of the fluorophore core and various functional groups tailored towards specific imaging requirements without worries about the functional group compatibilities and tedious aqueous purification during the synthesis of the fluorophore core. While our current tetravalent modification is expected to enhance targeting through avidity, it is also beneficial to explore other topology choices such as four water-solubilization groups and a single bioactive moiety. Our group is currently expanding the scope of both the packaged fluorophore core and other hydrophilic/bioactive functionalities to extend the platform for targeted and formulation-free SWIR imaging, with an overarching goal of providing user-friendly building blocks of SWIR detection reagents similar to the success of many commercially-available activated fluorophores in the visible region for easy bioconjugation. Finally, this fluorophore functionalization method on its two aniline groups also provides reference to future development of other aniline-containing molecules as modularized imaging agents and, more broadly, as other chemical biology tools.

Acknowledgement

This work was supported by the National Institutes of Health (1R01EB027172 to E.M.S.), Chan Zuckerberg Initiative (2020-225707 to E.M.S.), Tobacco Related Disease Research Program (T32DT4847 to E.Y.L) and UCLA (Dissertation Year Fellowship to I.L.). NMR spectrometers are supported by the National Science Foundation under equipment grant no. CHE-1048804. We would like to thank Dr. Philip Low and his group at Purdue University for providing OTL-38.

Graphical abstract

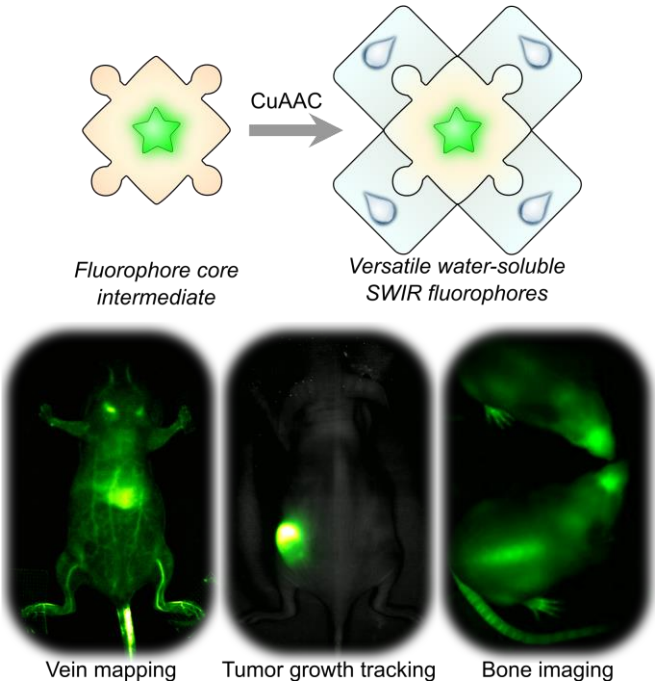

References

(1) Hong, G.; Antaris, A. L.; Dai, H. Near-Infrared Fluorophores for Biomedical Imaging. *Nat. Biomed. Eng.* **2017**, *1* (1), 1–22. https://doi.org/10.1038/s41551-016-0010.

(2) Thimsen, E.; Sadtler, B.; Berezin, M. Y. Shortwave-Infrared (SWIR) Emitters for Biological Imaging: A Review of Challenges and Opportunities. *Nanophotonics* **2017**, *6* (5), 1043–1054. https://doi.org/10.1515/nanoph-2017-0039.

(3) Li, C.; Chen, G.; Zhang, Y.; Wu, F.; Wang, Q. Advanced Fluorescence Imaging Technology in the Near-Infrared-II Window for Biomedical Applications. *J. Am. Chem. Soc.* **2020**, *142* (35), 14789–14804. https://doi.org/10.1021/jacs.0c07022.

(4) Lim, Y. T.; Kim, S.; Nakayama, A.; Stott, N. E.; Bawendi, M. G.; Frangioni, J. V. Selection of Quantum Dot Wavelengths for Biomedical Assays and Imaging. *Mol. Imaging* **2003**, *2* (1), 15353500200302164. https://doi.org/10.1162/15353500200302163.

(5) Diao, S.; Hong, G.; Antaris, A. L.; Blackburn, J. L.; Cheng, K.; Cheng, Z.; Dai, H. Biological Imaging without Autofluorescence in the Second Near-Infrared Region. *Nano Res.* **2015**, *8* (9), 3027–3034. https://doi.org/10.1007/s12274-015-0808-9.

(6) Del Rosal, B.; Villa, I.; Jaque, D.; Sanz-Rodríguez, F. In Vivo Autofluorescence in the Biological Windows: The Role of Pigmentation. *J. Biophotonics* **2016**, *9* (10), 1059–1067. https://doi.org/10.1002/jbio.201500271.

(7) Welsher, K.; Liu, Z.; Sherlock, S. P.; Robinson, J. T.; Chen, Z.; Daranciang, D.; Dai, H. A Route to Brightly Fluorescent Carbon Nanotubes for Near-Infrared Imaging in Mice. *Nat. Nanotechnol.* **2009**, *4* (11), 773–780. https://doi.org/10.1038/nnano.2009.294.

(8) Hu, Z.; Fang, C.; Li, B.; Zhang, Z.; Cao, C.; Cai, M.; Su, S.; Sun, X.; Shi, X.; Li, C.; Zhou, T.; Zhang, Y.; Chi, C.; He, P.; Xia, X.; Chen, Y.; Gambhir, S. S.; Cheng, Z.; Tian, J. First-in-Human Liver-Tumour Surgery Guided by Multispectral Fluorescence Imaging in the Visible and near-Infrared-I/II Windows. *Nat. Biomed. Eng.* **2020**, *4* (3), 259–271. https://doi.org/10.1038/s41551-019-0494-0.

(9) Bricks, J. L.; Kachkovskii, A. D.; Slominskii, Y. L.; Gerasov, A. O.; Popov, S. V. Molecular Design of near Infrared Polymethine Dyes: A Review. *Dyes Pigm.* **2015**, *121*, 238–255. https://doi.org/10.1016/j.dyepig.2015.05.016.

(10) Tatikolov, A. S. Polymethine Dyes as Spectral-Fluorescent Probes for Biomacromolecules. *J. Photochem. Photobiol. C Photochem. Rev.* **2012**, *13* (1), 55–90. https://doi.org/10.1016/j.jphotochemrev.2011.11.001.

(11) Gorka, A. P.; Nani, R. R.; Schnermann, M. J. Cyanine Polyene Reactivity: Scope and Biomedical Applications. *Org. Biomol. Chem.* **2015**, *13* (28), 7584–7598. https://doi.org/10.1039/c5ob00788g.

(12) Ma, X.; Shi, L.; Zhang, B.; Liu, L.; Fu, Y.; Zhang, X. Recent Advances in Bioprobes and Biolabels Based on Cyanine Dyes. *Anal. Bioanal. Chem.* **2022**, *414* (16), 4551–4573. https://doi.org/10.1007/s00216-022-03995-8.

(13) Swamy, M. M. M.; Murai, Y.; Monde, K.; Tsuboi, S.; Jin, T. Shortwave-Infrared Fluorescent Molecular Imaging Probes Based on π-Conjugation Extended Indocyanine Green. *Bioconjug. Chem.* **2021**, *32* (8), 1541–1547. https://doi.org/10.1021/acs.bioconjchem.1c00253.

(14) Bandi, V. G.; Luciano, M. P.; Saccomano, M.; Patel, N. L.; Bischof, T. S.; Lingg, J. G. P.; Tsrunchev, P. T.; Nix, M. N.; Ruehle, B.; Sanders, C.; Riffle, L.; Robinson, C. M.; Difilippantonio, S.; Kalen, J. D.; Resch-Genger, U.; Ivanic, J.; Bruns, O. T.; Schnermann, M. J. Targeted Multicolor in Vivo Imaging over 1,000 Nm Enabled by Nonamethine Cyanines. *Nat. Methods* **2022**, *19* (3), 353–358. https://doi.org/10.1038/s41592-022-01394-6.

(15) Zhu, S.; Tian, R.; Antaris, A. L.; Chen, X.; Dai, H. Near-Infrared-II Molecular Dyes for Cancer Imaging and Surgery. *Adv. Mater.* **2019**, *31* (24), 1900321. https://doi.org/10.1002/adma.201900321.

(16) Lei, Z.; Zhang, F. Molecular Engineering of NIR-II Fluorophores for Improved Biomedical Detection. *Angew. Chem. Int. Ed.* **2021**, *60* (30), 16294–16308. https://doi.org/10.1002/anie.202007040.

(17) Wong, K. C. Y.; Sletten, E. M. Extending Optical Chemical Tools and Technologies to Mice by Shifting to the Shortwave Infrared Region. *Curr. Opin. Chem. Biol.* **2022**, *68*, 102131. https://doi.org/10.1016/j.cbpa.2022.102131.

(18) Tolbert, L. M.; Zhao, X. Beyond the Cyanine Limit: Peierls Distortion and Symmetry Collapse in a Polymethine Dye. *J. Am. Chem. Soc.* **1997**, *119* (14), 3253–3258. https://doi.org/10.1021/ja9626953.

(19) Terenziani, F.; Przhonska, O. V.; Webster, S.; Padilha, L. A.; Slominsky, Y. L.; Davydenko, I. G.; Gerasov, A. O.; Kovtun, Y. P.; Shandura, M. P.; Kachkovski, A. D.; Hagan, D. J.; Van Stryland, E. W.; Painelli, A. Essential-State Model for Polymethine Dyes: Symmetry Breaking and Optical

Spectra. *J. Phys. Chem. Lett.* **2010**, *1* (12), 1800–1804. https://doi.org/10.1021/jz100430x.

(20) Li, B.; Lu, L.; Zhao, M.; Lei, Z.; Zhang, F. An Efficient 1064 Nm NIR-II Excitation Fluorescent Molecular Dye for Deep-Tissue High-Resolution Dynamic Bioimaging. *Angew. Chem. Int. Ed.* **2018**, *57* (25), 7483–7487. https://doi.org/10.1002/anie.201801226.

(21) Li, B.; Zhao, M.; Feng, L.; Dou, C.; Ding, S.; Zhou, G.; Lu, L.; Zhang, H.; Chen, F.; Li, X.; Li, G.; Zhao, S.; Jiang, C.; Wang, Y.; Zhao, D.; Cheng, Y.; Zhang, F. Organic NIR-II Molecule with Long Blood Half-Life for in Vivo Dynamic Vascular Imaging. *Nat. Commun.* **2020**, *11* (1), 3102. https://doi.org/10.1038/s41467-020-16924-z.

(22) Cosco, E. D.; Caram, J. R.; Bruns, O. T.; Franke, D.; Day, R. A.; Farr, E. P.; Bawendi, M. G.; Sletten, E. M. Flavylium Polymethine Fluorophores for Near- and Shortwave Infrared Imaging. *Angew. Chem. Int. Ed.* **2017**, *56* (42), 13126–13129. https://doi.org/10.1002/anie.201706974.

(23) Cosco, E. D.; Spearman, A. L.; Ramakrishnan, S.; Lingg, J. G. P.; Saccomano, M.; Pengshung, M.; Arús, B. A.; Wong, K. C. Y.; Glasl, S.; Ntziachristos, V.; Warmer, M.; McLaughlin, R. R.; Bruns, O. T.; Sletten, E. M. Shortwave Infrared Polymethine Fluorophores Matched to Excitation Lasers Enable Non-Invasive, Multicolour in Vivo Imaging in Real Time. *Nat. Chem.* **2020**, *12* (12), 1123–1130. https://doi.org/10.1038/s41557-020-00554-5.

(24) Cosco, E. D.; Arús, B. A.; Spearman, A. L.; Atallah, T. L.; Lim, I.; Leland, O. S.; Caram, J. R.; Bischof, T. S.; Bruns, O. T.; Sletten, E. M. Bright Chromenylium Polymethine Dyes Enable Fast, Four-Color In Vivo Imaging with Shortwave Infrared Detection. *J. Am. Chem. Soc.* **2021**, *143* (18), 6836–6846. https://doi.org/10.1021/jacs.0c11599.

(25) Pengshung, M.; Li, J.; Mukadum, F.; Lopez, S. A.; Sletten, E. M. Photophysical Tuning of Shortwave Infrared Flavylium Heptamethine Dyes via Substituent Placement. *Org. Lett.* **2020**, *22* (15), 6150–6154. https://doi.org/10.1021/acs.orglett.0c02213.

(26) Wang, S.; Fan, Y.; Li, D.; Sun, C.; Lei, Z.; Lu, L.; Wang, T.; Zhang, F. Anti-Quenching NIR-II Molecular Fluorophores for in Vivo High-Contrast Imaging and PH Sensing. *Nat. Commun.* **2019**, *10* (1), 1058. https://doi.org/10.1038/s41467-019-09043-x.

(27) Lei, Z.; Sun, C.; Pei, P.; Wang, S.; Li, D.; Zhang, X.; Zhang, F. Stable, Wavelength-Tunable Fluorescent Dyes in the NIR-II Region for In Vivo High-Contrast Bioimaging and Multiplexed Biosensing. *Angew. Chem. Int. Ed.* **2019**, *58* (24), 8166–8171. https://doi.org/10.1002/anie.201904182.

(28) He, Y.; Wang, S.; Yu, P.; Yan, K.; Ming, J.; Yao, C.; He, Z.; El-Toni, A. M.; Khan, A.; Zhu, X.; Sun, C.; Lei, Z.; Zhang, F. NIR-II Cell Endocytosis-Activated Fluorescent Probes for in Vivo High-Contrast Bioimaging Diagnostics. *Chem. Sci.* **2021**, *12* (31), 10474–10482. https://doi.org/10.1039/D1SC02763H.

(29) Urano, Y.; Kamiya, M.; Kanda, K.; Ueno, T.; Hirose, K.; Nagano, T. Evolution of Fluorescein as a Platform for Finely Tunable Fluorescence Probes. *J. Am. Chem. Soc.* **2005**, *127* (13), 4888–4894. https://doi.org/10.1021/ja043919h.

(30) Seijas, J. A.; Vázquez-Tato, M. P.; Carballido-Reboredo, R. Solvent-Free Synthesis of Functionalized Flavones under Microwave Irradiation. *J. Org. Chem.* **2005**, *70* (7), 2855–2858.

https://doi.org/10.1021/jo048685z.
(31) Hong, V.; Presolski, S. I.; Ma, C.; Finn, M. G. Analysis and Optimization of Copper-Catalyzed Azide–Alkyne Cycloaddition for Bioconjugation. *Angew. Chem. Int. Ed Engl.* **2009**, *48* (52), 9879–9883. https://doi.org/10.1002/anie.200905087.
(32) Cosco, E. D.; Lim, I.; Sletten, E. M. Photophysical Properties of Indocyanine Green in the Shortwave Infrared Region. *ChemPhotoChem* **2021**, *5* (8), 727–734. https://doi.org/10.1002/cptc.202100045.
(33) Gathje, J.; Steuer, R. R.; Nicholes, K. R. Stability Studies on Indocyanine Green Dye. *J. Appl. Physiol.* **1970**, *29* (2), 181–185. https://doi.org/10.1152/jappl.1970.29.2.181.
(34) Mindt, S.; Karampinis, I.; John, M.; Neumaier, M.; Nowak, K. Stability and Degradation of Indocyanine Green in Plasma, Aqueous Solution and Whole Blood. *Photochem. Photobiol. Sci.* **2018**, *17* (9), 1189–1196. https://doi.org/10.1039/C8PP00064F.
(35) Milesi-Hallé, A.; Abdel-Rahman, S. M.; Brown, A.; McCullough, S. S.; Letzig, L.; Hinson, J. A.; James, L. P. Indocyanine Green Clearance Varies as a Function of N-Acetylcysteine Treatment in a Murine Model of Acetaminophen Toxicity. *Chem. Biol. Interact.* **2011**, *189* (3), 222–229. https://doi.org/10.1016/j.cbi.2010.12.001.
(36) Carr, J. A.; Franke, D.; Caram, J. R.; Perkinson, C. F.; Saif, M.; Askoxylakis, V.; Datta, M.; Fukumura, D.; Jain, R. K.; Bawendi, M. G.; Bruns, O. T. Shortwave Infrared Fluorescence Imaging with the Clinically Approved Near-Infrared Dye Indocyanine Green. *Proc. Natl. Acad. Sci.* **2018**, *115* (17), 4465–4470. https://doi.org/10.1073/pnas.1718917115.
(37) van Manen, L.; Handgraaf, H. J. M.; Diana, M.; Dijkstra, J.; Ishizawa, T.; Vahrmeijer, A. L.; Mieog, J. S. D. A Practical Guide for the Use of Indocyanine Green and Methylene Blue in Fluorescence-guided Abdominal Surgery. *J. Surg. Oncol.* **2018**, *118* (2), 283–300. https://doi.org/10.1002/jso.25105.
(38) Gao, S.; Yu, Y.; Wang, Z.; Wu, Y.; Qiu, X.; Jian, C.; Yu, A. NIR-II Fluorescence Imaging Using Indocyanine Green Provides Early Prediction of Skin Avulsion-Injury in a Porcine Model. *Clin. Cosmet. Investig. Dermatol.* **2022**, *15*, 447–454. https://doi.org/10.2147/CCID.S357989.
(39) Carr, J. A.; Aellen, M.; Franke, D.; So, P. T. C.; Bruns, O. T.; Bawendi, M. G. Absorption by Water Increases Fluorescence Image Contrast of Biological Tissue in the Shortwave Infrared. *Proc. Natl. Acad. Sci.* **2018**, *115* (37), 9080–9085. https://doi.org/10.1073/pnas.1803210115.
(40) Dhaliwal, K.; Escher, G.; Unciti-Broceta, A.; McDonald, N.; Simpson, A. J.; Haslett, C.; Bradley, M. Far Red and NIR Dye-Peptoid Conjugates for Efficient Immune Cell Labelling and Tracking in Preclinical Models. *MedChemComm* **2011**, *2* (11), 1050–1053. https://doi.org/10.1039/C1MD00171J.
(41) Wang, L.; Xia, Q.; Hou, M.; Yan, C.; Xu, Y.; Qu, J.; Liu, R. A Photostable Cationic Fluorophore for Long-Term Bioimaging. *J. Mater. Chem. B* **2017**, *5* (46), 9183–9188. https://doi.org/10.1039/C7TB02668D.
(42) Chen, G.; Zhang, Y.; Li, C.; Huang, D.; Wang, Q.; Wang, Q. Recent Advances in Tracking the Transplanted Stem Cells Using Near-Infrared Fluorescent Nanoprobes: Turning from the First to

the Second Near-Infrared Window. *Adv. Healthc. Mater.* **2018**, *7* (20), 1800497. https://doi.org/10.1002/adhm.201800497.

(43) Mahalingam, S. M.; Kularatne, S. A.; Myers, C. H.; Gagare, P.; Norshi, M.; Liu, X.; Singhal, S.; Low, P. S. Evaluation of Novel Tumor-Targeted Near-Infrared Probe for Fluorescence-Guided Surgery of Cancer. *J. Med. Chem.* **2018**, *61* (21), 9637–9646. https://doi.org/10.1021/acs.jmedchem.8b01115.

(44) McClung, M.; Harris, S. T.; Miller, P. D.; Bauer, D. C.; Davison, K. S.; Dian, L.; Hanley, D. A.; Kendler, D. L.; Yuen, C. K.; Lewiecki, E. M. Bisphosphonate Therapy for Osteoporosis: Benefits, Risks, and Drug Holiday. *Am. J. Med.* **2013**, *126* (1), 13–20. https://doi.org/10.1016/j.amjmed.2012.06.023.

(45) Zaheer, A.; Lenkinski, R. E.; Mahmood, A.; Jones, A. G.; Cantley, L. C.; Frangioni, J. V. In Vivo Near-Infrared Fluorescence Imaging of Osteoblastic Activity. *Nat. Biotechnol.* **2001**, *19* (12), 1148–1154. https://doi.org/10.1038/nbt1201-1148.

(46) Bhushan, K. R.; Misra, P.; Liu, F.; Mathur, S.; Lenkinski, R. E.; Frangioni, J. V. Detection of Breast Cancer Microcalcifications Using a Dual-Modality SPECT/NIR Fluorescent Probe. *J. Am. Chem. Soc.* **2008**, *130* (52), 17648–17649. https://doi.org/10.1021/ja807099s.

(47) Hyun, H.; Wada, H.; Bao, K.; Gravier, J.; Yadav, Y.; Laramie, M.; Henary, M.; Frangioni, J. V.; Choi, H. S. Phosphonated Near-Infrared Fluorophores for Biomedical Imaging of Bone. *Angew. Chem. Int. Ed Engl.* **2014**, *53* (40), 10668–10672. https://doi.org/10.1002/anie.201404930.